ChemComm

COMMUNICATION

View Article Online
View Journal | View Issue

Cite this: *Chem. Commun.*, 2024, **60**, 14196

Received 25th September 2024,
Accepted 5th November 2024

DOI: 10.1039/d4cc04938a

rsc.li/chemcomm

An effective orange-red solution-processed circularly polarized organic light-emitting diode†

Junqing Wang,[a] Xiaoyi Lai,[a] Yongzhi Zhou,[ab] Lei Hua,[a] Weiguo Zhu,[a] Pengfei Duan *[b] and Yafei Wang *[a]

A pair of circularly polarized thermally activated delayed fluorescence (CP-TADF) materials (*R*)-ad-PXZ/(*S*)-ad-PXZ were obtained, which show orange-red emission at 602 nm and clear chiroptical properties both in solution and the solid state. The solution processable circularly polarized device exhibits the maximum external quantum efficiency of 9.0% and g_{EL} value of 10^{-3}.

Circularly polarized light-emitting diodes (CP-OLEDs) have attracted much attention from both academia and industry due to their directly emissive circularly polarized electroluminescence,[1–3] which can effectively work with an antiglare polarizer to match its transmitted light handedness and then improve the device performance. Over the past decade, considerable CP-OLEDs with the emission colour spanning from the blue to red region have been achieved.[4,5] To date, a circularly polarized luminescent emitter is the most efficient candidate for realizing CP-OLEDs.

Since the seminal report by Adachi's group,[6] thermally activated delayed fluorescent (TADF) materials have become the most popular candidate for OLEDs due to their harvesting both singlet and triplet excitons and metal-free atoms. Integrating the chiral unit into the TADF emitter, named circularly polarized TADF (CP-TADF), is an effective path to obtain a chiral emitter. Substantial efforts have been made to realize CP-TADF emitters through chiral perturbation and intrinsic chiral strategies.[7–9] However, orange-red/red CP-TADF emitters with the emission wavelength above 580 nm still lag far behind blue and green CP-TADF emitters. Most reported orange-red/red CP-TADF emitters are composed of a chiral unit and a red TADF chromophore. For example, some groups integrated octahydro-1,1′-binaphthalene/or binaphthalene units into the red TADF chromophore with phenazine/benzothiadiazole/tetracoordinate boron complex fragments.[10–13] In addition, helicene analogues were also reported for red CP-TADF, which achieved impressive device performance and circularly polarized electroluminescence (CPEL).[14] Recently, Cheng and co-workers developed a charming strategy for an orange-red CP-TADF emitter through a chiral acceptor fragment. Although the device showed a low maximum external quantum efficiency (EQE_{max}) of 1.8%,[15] it provided an avenue to design red CP-TADF emitters. Unfortunately, few orange-red/red CP-OLEDs have been fabricated *via* solution processable methods because of the poor solubility caused by their rigid skeleton. Thus, it is necessary to develop solution-processed CP-OLEDs with long-wavelength emission.

In view of acridone and quinacridone having outstanding electron-withdrawing properties,[16] herein, a novel chiral acceptor unit combination of binaphthalene and acridone was proposed. Compared to the xanthenone-based chiral acceptor,[15] the nitrogen atom replacement of the oxygen atom can effectively modify the electronic properties, and then improve the device performance. To this end, two novel orange-red CP-TADF emitters, called **(*R*)-ad-PXZ**/**(*S*)-ad-PXZ** (Fig. 1), were prepared, in which the phenothiazine (PXZ) was used as a donor and the binaphthalene–acridone derivative as the acceptor fragment. Using the chiral compound as the emissive layer, an impressive solution-processable orange-red CP-OLED with an EQE_{max} of 9.0%, and a conspicuous g_{EL} value of *ca.* 1.3×10^{-3} was obtained. This result clearly demonstrates that the precise manipulation of the chiral acceptor skeleton can skillfully provide a better example of a solution-processed orange-red emitter.

As shown in Scheme S1 (ESI†), a pair of chiral acceptors **(*R*)-4**/**(*S*)-4** was synthesized by successive Buchwald–Hartwig coupling and Friedel–Crafts acylation reaction. The target compounds **(*R*)-ad-PXZ**/**(*S*)-ad-PXZ** were prepared by Buchwald–Hartwig coupling reaction between **(*R*)-4**/**(*S*)-4** and phenoxazine (PXZ), which were confirmed by ^{1}H NMR, ^{13}C NMR and MALDI-TOF mass spectrometry (Fig. S1–S14, ESI†). The enantiomers exhibit excellent thermal stability with high decomposition temperature (T_d, at 5% weight loss) of 459 °C and a glass transition temperature of 230 °C (T_g) (Fig. S15, ESI†). In addition, **(*R*)-ad-PXZ**/**(*S*)-ad-PXZ** possesses

[a] *School of Materials Science & Engineering, Jiangsu Collaborative Innovation Center of Photovoltaic Science and Engineering, Jiangsu Engineering Laboratory of Light-Electricity-Heat Energy-Converting Materials and Applications, Changzhou University, Changzhou 213164, P. R. China. E-mail: qiji830404@hotmail.com*

[b] *CAS Key Laboratory of Nanosystem and Hierarchical Fabrication, National Center for Nanoscience and Technology (NCNST), No. 11, ZhongGuanCun BeiYiTiao, Beijing 100190, P. R. China. E-mail: duanpf@nanoctr.cn*

† Electronic supplementary information (ESI) available. See DOI: https://doi.org/10.1039/d4cc04938a

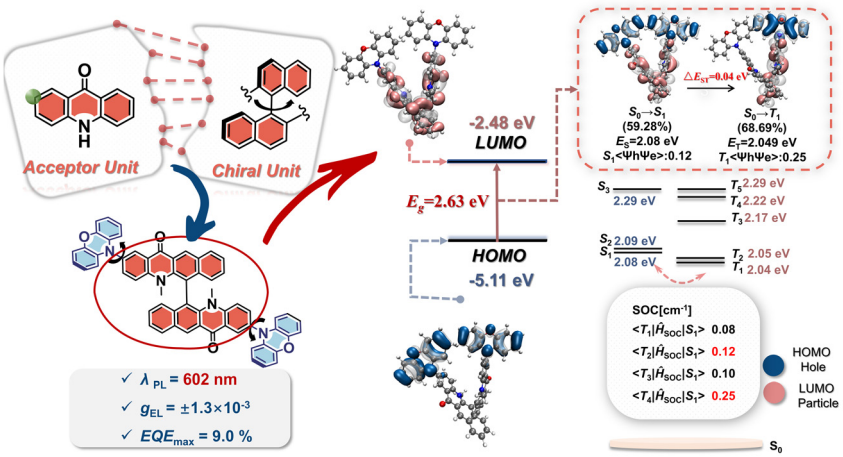

Fig. 1 Schematic diagram of the molecular design concepts for CP-TADF involved in this work and chemical structures of the enantiomer, and theoretical simulation of the ground and excited states for **(*R*)-ad-PXZ**. Contours and energy levels of the first FMOs for ground-state (S_0) **(*R*)-ad-PXZ** and their contributions to the first singlet and triple excitations. HOMO and LUMO refer to the highest occupied and lowest unoccupied molecular orbitals, respectively. Contours of the "hole" and "particle" and transition parameters for these excitations simulated with natural transition orbital (NTO) analysis (center in boxes). *E*, and $\langle \Psi_h \Psi_e \rangle$ refer to the excited-state energy level, and the overlap integral, respectively. The subscripts of S and T refer to singlet and triplet states, respectively.

good solubility in common organic solvents, such as dichloromethane, chloroform and THF and so on.

The electrochemical behaviours of the enantiomers show that only quasi-reversible oxidation potential (E_{ox}) was detected for the enantiomers (Fig. S16, ESI†). The HOMO (highest occupied molecular orbital) energy level of **(*R*)-ad-PXZ** is calculated to be −4.86 eV according to the empirical formula of $E_{HOMO} = -(E_{ox} + 4.8)$ eV. Based on the HOMO level and optical bandgap (Fig. 2a, 2.08 eV), the LUMO (lowest unoccupied molecular orbital) energy level of **(*R*)-ad-PXZ** is estimated to be −2.78 eV.

To elucidate the underlying principles of the molecular design concepts, density functional theory (DFT) calculations at the level of PBE1PBE/6-311g(d,p) were carried out. As shown in Fig. 1 and Fig. S17 (ESI†), the chiral emitters exhibit a twisted molecular geometry. The HOMO is mainly localized on the phenoxazine unit, while the LUMO is distributed on both the binaphthalene and acridone fragments. Such results suggest the participation of the chiral moiety in the chromophore, enabling effective chiroptical properties. In addition, the spatially separated HOMO and LUMO implies a small energy difference between singlet (S_1) and triplet (T_1) states (ΔE_{ST}) in the chiral emitters.

The natural transition orbitals (NTO) analysis was then calculated by using time-dependent DFT (TD-DFT) and Multiwfn. The $S_0 \rightarrow S_1$ excitations reflect the charge transfer (CT) property, similarly in the T_1 state. A relatively small ΔE_{ST} value of 0.04 eV was calculated, implying a reasonable TADF channel. Meanwhile, the $S_0 \rightarrow T_4$ excitations mean the predominant localized excited (LE) state, providing a large SOC value, and then accelerate the triplet-to-singlet spin flip processes.[17]

Due to the enantiomer structure, only **(*R*)-ad-PXZ** will be discussed in detail in the main text, and the other one is presented in the ESI† (Fig. S19 and Table S1). The steady-state absorption and photoluminescence (PL) properties of **(*R*)-ad-PXZ** were measured in toluene solution and a doped 4,4′,4″-tris(carbazol-9-yl)-triphenylamine (TCTA) film at room temperature, and the relevant data are summarized in Table S1 (ESI†). As shown in Fig. 2a, the intense absorption bands in the range of 280–310 nm are attributed to π–π* transitions of the aromatic system, while the strong absorption band at *ca.* 450 nm is associated with the intramolecular CT (ICT) processes. Intense orange-red emission with a peak at 602 nm was detected for **(*R*)-ad-PXZ** in the toluene solution. Such broad and structureless PL profile demonstrates the emission originating from CT transition. The obvious solvatochromic effect also confirms the CT feature in the chiral emitters (Fig. S19e and f, ESI†). Compared to the emission in solution, the doped film with 10 wt% **(*R*)-ad-PXZ** in TCTA was blue-shifted to 596 nm, probably attributed to the reduced ICT effect and dipole–dipole interactions caused by the nonpolar

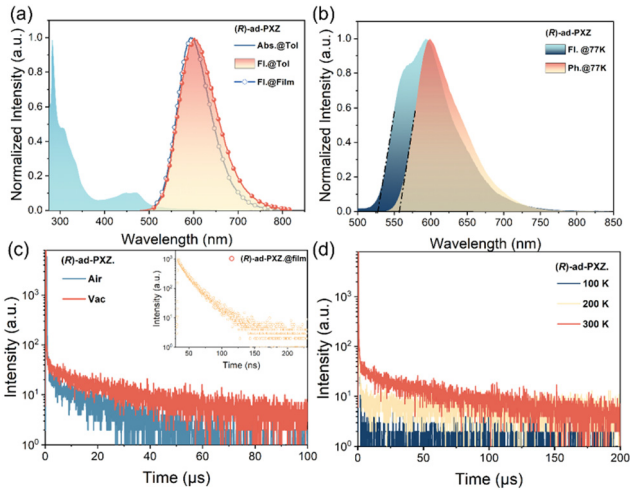

Fig. 2 (a) UV-vis absorption and PL spectra of **(*R*)-ad-PXZ** in toluene (10^{-5} M) and 10 wt% **(*R*)-ad-PXZ** doped in TCTA (λ_{ex} = 450 nm); (b) fluorescence and phosphorescence spectra of **(*R*)-ad-PXZ** in toluene at 77 K (λ_{ex} = 450 nm); (c) transient PL spectra of the doped films of **(*R*)-ad-PXZ** in air and under vacuum (Inset: Prompt PL decay curves measured in a time window of 200 ns) (λ_{ex} = 365 nm); (d) temperature-dependent transient PL decay spectra of the **(*R*)-ad-PXZ** doped film (λ_{ex} = 365 nm).

matrix environment of the TCTA host. The PLQY of the **(*R*)-ad-PXZ** was measured to be 15.8% in the doped film.

The S_1 and T_1 energy levels of **(*R*)-ad-PXZ** were determined by the onset positions of the low-temperature (LT) fluorescence (Fl) and phosphorescence (Ph) spectra at 77 K, respectively (Fig. 2b). Correspondingly, a small ΔE_{ST} value of 0.10 eV was calculated for **(*R*)-ad-PXZ** in solution, implying a probably RISC process. On the other hand, 10 wt% doped films of **(*R*)-ad-PXZ** in TCTA also displayed the small ΔE_{ST} values of *ca.* 0.06 eV (Fig. S20, ESI†). The time-resolved PL decays of such doped films show clear both prompt and delayed PL under vacuum conditions (Fig. 2c). The prompt PL reveals a lifetime (τ_p) of 21.0 ns, while the delayed fluorescence lifetime (τ_d) is evaluated to be *ca.* 52.0 μs. The delayed emission is significantly quenched in the presence of air, confirming the involvement of triplet excitons in the emission process. The temperature-dependent time-resolved PL decays demonstrate that the delayed emission component noticeably increases with increasing temperature from 100 K to 300 K (Fig. 2d), indicating the presence of TADF.

As depicted in Fig. 3a, the electronic circular dichroism (ECD) spectra of enantiomeric pairs display a mirror image behaviour in toluene solution. Similar to the absorption spectra (Fig. 2a), the Cotton effects observed at longer wavelengths around 450 nm can be attributed to the ICT transition between the chiral binaphthyl acceptor and PXZ donor units. Impressively, the ECD spectrum of **(*R*)-ad-PXZ** obtained by theoretical simulations is similar to the experimental result. The CD results confirm that the chirality property of **(*R*)-ad-PXZ**/**(*S*)-ad-PXZ** is reliably ensured in the ground state. The CPL spectra of both emitters were subsequently detected in toluene and doped films (10 wt% in TCTA) to explore their chiroptical behaviours in excited states (Fig. 3b and c). It is worth noting that mirror-image and unstructured CPL with peaks at about 632 nm and 587 nm are observed for the enantiomers both in solution and the solid state. In solution, the corresponding g_{PL} values are +2.8 × 10^{-3}/−2.9 × 10^{-3} for **(*R*)-ad-PXZ**/**(*S*)-ad-PXZ**, respectively (Fig. 3d). According to the formula of $B_{CPL} = \varepsilon \times \Phi \times |g_{lum}|/2$, the CPL brightness values, which are defined to evaluate the performance of CPL materials, were calculated to be 0.23 for **(*R*)-ad-PXZ** and 0.30 M^{-1} cm^{-1} for **(*S*)-ad-PXZ**.[18] As for the 10 wt% doped films of the emitter in TCTA, the g_{PL} values are +5.8 × 10^{-3}/−6.4 × 10^{-3} for **(*R*)-ad-PXZ**/**(*S*)-ad-PXZ**, respectively. Obviously, constructing a chiral acceptor moiety is an effective strategy for realizing CPL, thereby facilitating the fulfilment of CP-OLED requirements.

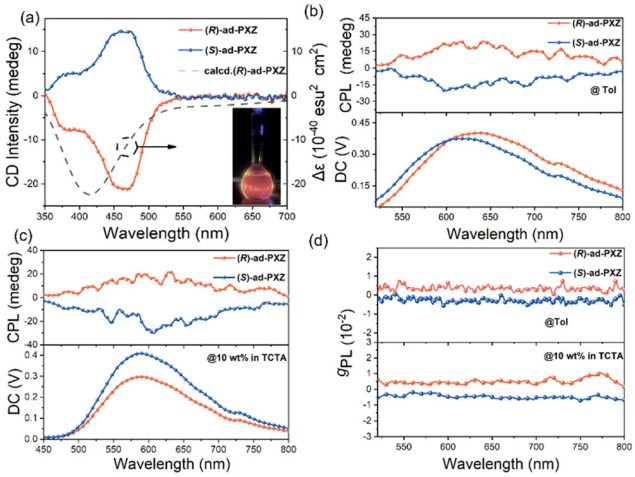

Fig. 3 (a) Experimental and calculated ECD spectra of **(*R*)-ad-PXZ**/**(*S*)-ad-PXZ** in toluene (1.0 × 10^{-5} mol L^{-1}); (b) CPL spectra and DC spectra of **(*R*)-ad-PXZ**/**(*S*)-ad-PXZ** in toluene (1.0 × 10^{-5} mol L^{-1}) (λ_{ex} = 365 nm); (c) CPL spectra and DC spectra of 10 wt% **(*R*)-ad-PXZ**/**(*S*)-ad-PXZ** in TCTA (λ_{ex} = 365 nm); (d) g_{PL} *versus* wavelength curves of **(*R*)-ad-PXZ**/**(*S*)-ad-PXZ** in toluene (1.0 × 10^{-5} mol L^{-1}) and the doped film (10 wt% in TCTA).

In order to evaluate the electroluminescent (EL) properties of the chiral emitters, solution-processable CP-OLEDs with the device configuration of ITO/PEDOT:PSS (poly(3,4-ethylenedioxythiophene)/poly(styrenesulfonate), 35 nm)/PVK (poly(*N*-vinylcarbazole, 60 nm)/EML (25 nm))/DPEPO (bis[2-(triphenyl-phosphine)phenyl] ether oxide, 6 nm)/TmPyPB (1,3,5-tri(*m*-pyrid-3-yl-phenyl)benzene, 48 nm)/LiF (0.5 nm)/Al (120 nm) were fabricated (Fig. 4a). Herein, TCTA was selected as the host material owing to its high triplet energy level, good hole transport ability and excellent solution processability. The emitting layer (EML) is composed of chiral compounds and a TCTA host, and the dopant concentrations are 5, 10 and 15 wt% (the optimized dopant concentration is 10 wt%). The **(*R*)-ad-PXZ** and **(*S*)-ad-PXZ** based devices show analogous emission spectra with those of PL profiles (Fig. 4b and Fig. S21c, ESI†), implying that there is a complete energy transfer between TCTA and the chiral dopant. With increasing dopant concentration, the EL spectra exhibit a red shift due to the increased intermolecular interaction. When the dopant concentration is 10 wt%, the **(*R*)-ad-PXZ** based device possesses the best performance with the maximum brightness (L_{max}) of 1385 cd m^{-2}, maximum current efficiency (CE_{max}) of 12.83 cd A^{-1}, and maximum external quantum efficiency (EQE_{max}) of 5.8% (Fig. 4c, d and Table S3, ESI†).

Encouraged by the strategy of TADF-sensitized high-efficiency OLEDs, DtBuCzB (2,6-bis(3,6-di-*tert*-butyl-9*H*-carbazol-9-yl)boron) is anticipated to work as a sensitizer due to its fast RISC process and high emission efficiency. The obvious overlaps between the fluorescence spectrum of DtBuCzB and absorption of **(*R*)-ad-PXZ** suggest that there is an effective Förster resonance energy transfer (FRET) between DtBuCzB and the terminal emitter (Fig. S22a, ESI†). The transient PL decay reveals that the delayed component increases significantly with the additional DtBuCzB in the chiral emitter and TACT system, also proving the FRET process between the sensitizer and chiral emitter (Fig. S22b, ESI†). To this end, the sensitized solution processable OLED with the structure of ITO/PEDOT:PSS (35 nm)/PVK (30 nm)/EML (25 nm)/TmPyPB (48 nm)/LiF (0.5 nm)/Al (120 nm) was fabricated. In such a device, the EML is composed of host:sensitizer (20 wt%):chiral emitter (*x* wt%, *x* = 5, 7, 9, 11 wt%) (Fig. S23 and S24, ESI†). Compared to the non-sensitized devices, the sensitized devices show similar EL spectra, demonstrating the emission originating from the terminal chiral emitter (Fig. 4b). When the dopant concentration is 9 wt%, the sensitized device realizes an EQE_{max} of 9.0%, a CE_{max} of 20.4 cd A^{-1}, and a L_{max} of 2509 cd m^{-2} (Fig. 4 and Table S4, ESI†), which is almost twice higher than that of non-sensitized devices. Then the circularly polarized electroluminescence (CPEL) properties of the devices with/without sensitizer were explored, and all devices present clear CPEL

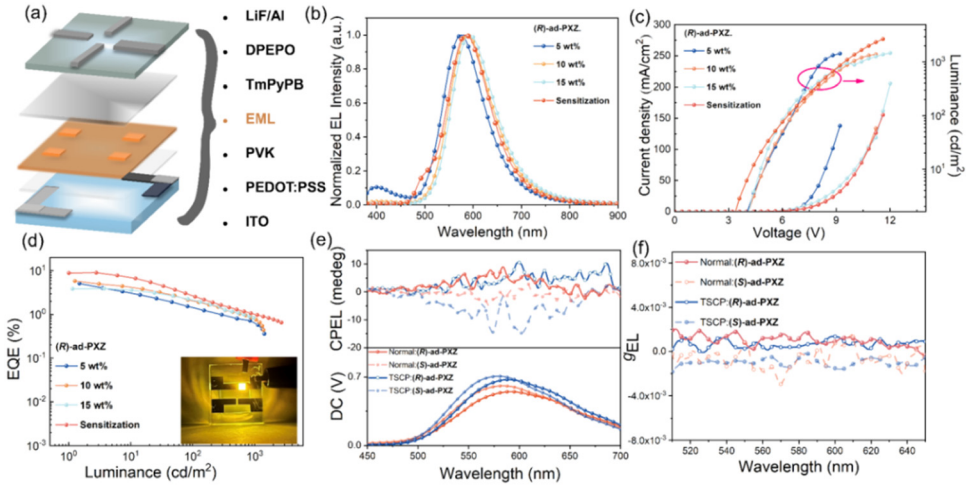

Fig. 4 (a) The structures of the solution-processable OLED materials; (b) normalized EL spectra of **(*R*)-ad-PXZ**; (c) current density–voltage–luminance (*J*–*V*–*L*) characteristics; (d) external quantum efficiency *versus* luminance (EQE–*L*) curves; (e) CPEL spectra and DC spectra of **(*R*)-ad-PXZ/(*S*)-ad-PXZ**; (f) g_{EL} spectra of **(*R*)-ad-PXZ/(*S*)-ad-PXZ**.

signals. As for the non-sensitized CP-OLEDs, the asymmetry factors (g_{EL}) are +1.3 × 10^{-3} at 599 nm and −1.2× 10^{-3} at 595 nm for **(*R*)-ad-PXZ** and **(*S*)-ad-PXZ** based devices, respectively. As for the sensitized CP-OLEDs, the g_{EL} values are detected to be +1.4 × 10^{-3} at 584 nm and −1.4 × 10^{-3} at 577 nm for **(*R*)-ad-PXZ** and **(*S*)-ad-PXZ**, respectively (Fig. 4d and f). It is worth noting that the g_{EL} of the device is significantly smaller than that of the g_{PL} in doped films, which can be ascribed to the reflection effect from the cathode electrode.[19] To better evaluate the comprehensive performance of CPEL materials, the *Q*-factor, defined as |EQE × g_{EL}|, was determined to be 0.1 × 10^{-3} for the CP-OLEDs.[20] The above results indicate that the utilization of the TADF-sensitizer emitter in CP-OLED can effectively enhance the device performance.

In summary, efficient orange-red CP-TADF emitters **(*R*)-ad-PXZ/(*S*)-ad-PXZ** were prepared through the chiral acceptor strategy. Both the emitters possessed a low ΔE_{ST} value and showed emission at 602 nm in the toluene solution. Clear chiral optical activity with $|g_{PL}|$ of 10^{-3} is observed both in solution and the solid state. Employing such chiral emitters as the dopant, solution processable CP-OLEDs were achieved with an EQE_{max} of 9.0% and $|g_{EL}|$ of *ca.* 1.3 × 10^{-3}. This study provides an effective method for designing soluble orange-red CP-TADF emitters.

This work was financially supported by the National Natural Science Foundation of China (No. 22371020, 52073035, 22405027); Special program for foreign talents in Changzhou City (CQ20224052); and the Natural Science Foundation of the Jiangsu Higher Education Institutions of China (24KJB150003). Meanwhile, we would like to acknowledge the help of Prof. Yuchao Liu from Qingdao University of Science and Technology with the photophysical characterization.

Data availability

The data supporting this article have been included as part of the ESI.†

Conflicts of interest

There are no conflicts to declare.

Notes and references

1 Z.-L. Gong, X. Zhu, Z. Zhou, S.-W. Zhang, D. Yang, B. Zhao, Y.-P. Zhang, J. Deng, Y. Cheng, Y.-X. Zheng, S.-Q. Zang, H. Kuang, P. Duan, M. Yuan, C.-F. Chen, Y. S. Zhao, Y.-W. Zhong, B. Z. Tang and M. Liu, *Sci. China*, 2021, **64**, 2060–2104.
2 J. Han, S. Guo, H. Lu, S. Liu, Q. Zhao and W. Huang, *Adv. Opt. Mater.*, 2018, **6**, 1800538.
3 Y. Sang, J. Han, T. Zhao, P. Duan and M. Liu, *Adv. Mater.*, 2020, **32**, 1900110.
4 L. Frédéric, A. Desmarchelier, L. Favereau and G. Pieters, *Adv. Funct. Mater.*, 2021, **31**, 2010281.
5 Z. P. Yan, L. Yuan, Y. Zhang, M. X. Mao, X. J. Liao, H. X. Ni, Z. H. Wang, Z. An, Y. X. Zheng and J. L. Zuo, *Adv. Mater.*, 2022, **34**, 2204253.
6 H. Uoyama, K. Goushi, K. Shizu, H. Nomura and C. Adachi, *Nature*, 2012, **492**, 234–238.
7 Y. Tsuchiya, Y. Ishikawa, S. H. Lee, X. K. Chen, J. L. Brédas, H. Nakanotani and C. Adachi, *Adv. Opt. Mater.*, 2021, **9**, 2002174.
8 B. He, Q. Zhong, Q. Dong, X. Yang, S. J. Cowling, W. Qiao, D. W. Bruce, W. Zhu, P. Duan and Y. Wang, *Mater. Horiz.*, 2024, **11**, 1251–1260.
9 Y. Y. Ju, L. E. Xie, J. F. Xing, Q. S. Deng, X. W. Chen, L. X. Huang, G. H. Nie, Y. Z. Tan and B. Zhang, *Angew. Chem., Int. Ed.*, 2024, e202414383.
10 M. Li and C.-F. Chen, *Org. Chem. Front.*, 2022, **9**, 6441–6452.
11 B. Sun, L. Ding, X. Wang, Z.-L. Tu and J. Fan, *Chem. Eng. J.*, 2023, **476**, 146511.
12 L. Zhou, F. Ni, N. Li, K. Wang, G. Xie and C. Yang, *Angew. Chem., Int. Ed.*, 2022, **61**, e202203844.
13 P. Xue, X. Wang, W. Wang, J. Zhang, Z. Wang, J. Jin, C. Zheng, P. Li, G. Xie and R. Chen, *ACS Appl. Mater. Interfaces*, 2021, **13**, 47826–47834.
14 L. Zhu, D. Liu, K. Wu, G. Xie, Z. Zhao and B. Z. Tang, *Chem. Res. Chin. Univ.*, 2024, **40**, 657–663.
15 W. C. Guo, W. L. Zhao, K. K. Tan, M. Li and C. F. Chen, *Angew. Chem., Int. Ed.*, 2024, **63**, e202401835.
16 Y. Wang, Y. Zhang, W. Hu, Y. Quan, Y. Li and Y. Cheng, *ACS Appl. Mater. Interfaces*, 2019, **11**, 26165–26173.
17 M. Guzauskas, D. Volyniuk, I. Kulszewicz-Bajer, M. Mahmoudi, A. Lazauskas, V. Jasinskas, V. Gulbinas, A. Pron and J. V. Grazulevicius, *Adv. Opt. Mater.*, 2023, **11**, 26165–26173.
18 L. Arrico, L. Di Bari and F. Zinna, *Chem. – Eur. J.*, 2021, **27**, 2920–2934.
19 F. Zinna, M. Pasini, F. Galeotti, C. Botta, L. Di Bari and U. Giovanella, *Adv. Funct. Mater.*, 2017, **27**, 1603719.
20 C. H. Guo, Y. Zhang, W. L. Zhao, K. K. Tan, L. Feng, L. Duan, C. F. Chen and M. Li, *Adv. Mater.*, 2024, **36**, 2406550.